Chapter

# Electrical Properties of Binary Thin Films

*Luminița Mirela Hrib, Liliana-Marinela Balescu, Cristina Florentina Chirila, Andra-Georgia Boni, Dana Georgeta Popescu, Marian Cosmin Istrate, Roxana Elena Patru, Lucia Nicoleta Leonat and Lucian Pintilie*

## Abstract

Binary compounds have been extensively studied in recent years due to their numerous advantageous characteristics, making them attractive to both industrial and academic research. Among these, doped hafnium oxide ($HfO_2$) and aluminum nitride (AlN) thin films are particularly promising because they are compatible with silicon technology, are environmentally safe and lead-free, and exhibit ferroelectric properties desirable for next-generation electronic devices such as nonvolatile memories and ferroelectric field-effect transistors. However, stabilizing the ferroelectric phase in these materials remains challenging because achieving the desired crystalline structure and optimal dopant incorporation requires precise control over deposition and processing parameters. In this chapter, experimental results on $Al_{1-x}Sc_xN$ and $Hf_{0.5}Zr_{0.5}O_2$ thin films are presented, with the primary aim of establishing correlations between preparation conditions and electrical properties. By systematically varying growth parameters and analyzing the resulting microstructure and functional responses, this study elucidates how processing influences phase formation, leakage behavior, and electrical properties in these emerging thin films, providing insights for their integration into future electronic device architectures.

**Keywords:** electrical properties, thin films, hafnium oxide, aluminum scandium nitride, sputtering, ferroelectric

## 1. Introduction

In recent years, the development of applications such as artificial intelligence, the internet of things, autonomous driving, social networks, and smart cities has increased the demand for advanced memory storage solutions. It is estimated that global data generation is increasing by multiple quintillions of bytes per day, creating an urgent need for new memory technologies that can store large amounts of information efficiently while operating at low power and high speed. To meet the

performance, power, and integration demands of next-generation data-centric computer systems, emerging memory ideas such as ferroelectric, resistive, and magnetic memory devices are being actively studied. The traditional functional materials used in memory and logic devices (such as ferroelectric perovskites) often have poor compatibility with silicon complementary metal–oxide–semiconductor (CMOS) fabrication processes, and they may contain toxic elements such as lead (e.g., $Pb(Zr,Ti)O_3$), which pose environmental risks. In addition, the functional performance of these materials degrades as their thickness is reduced to the nanometer scale: the coercive field [1, 2] and the leakage currents [3] tend to increase, thereby raising the risk of electrical breakdown. At the nanoscale, surface and size effects can significantly alter a material's free energy, enabling the stabilization of metastable phases in the bulk. This phenomenon opens the possibility of discovering new ferroelectrics among abundant, nontoxic, and inexpensive materials, broadening the scope of functional materials beyond traditional perovskite oxides. In this context, binary compounds are of particular interest because they often exhibit a great variety of polymorphs with distinct atomic coordinations, providing a rich set of metastable structures that may host polar and ferroelectric phases when appropriately engineered. For example, binary metal oxides such as $HfO_2$ and $ZrO_2$ – traditionally regarded as centrosymmetric dielectrics – can undergo size- or dopant-induced phase transitions to noncentrosymmetric orthorhombic structures that exhibit ferroelectric behavior at nanometer thicknesses [4, 5]. While in the most well-known ferroelectrics, the ferroelectric phase is stable at room temperature (RT) and atmospheric pressure, in $HfO_2$, the orthorhombic phase is metastable in bulk. Still, it can be stabilized in thin films through extrinsic contributions, such as chemical pressure from dopants, oxygen-vacancy engineering, interface-induced stress, and kinetic factors during processing [6, 7], which alter the surface energy. Also, the microscopic origin of polarization in $HfO_2$-based materials is different from that found in classical displacive ferroelectrics (e.g., $BaTiO_3$, $Pb(Zr,Ti)O_3$). In the polar orthorhombic phase of $HfO_2$, the ferroelectric polarization is largely driven by the displacement of oxygen anions, while the positions of the hafnium cations remain closer to those of the parent nonpolar phase. This anion-driven polarization mechanism makes ferroelectricity particularly sensitive to oxygen-vacancy concentration and the local defect landscape. Therefore, the ferroelectric phase exists within a relatively narrow processing window, and small deviations in temperature, dopant level, or stress can cause the film to relax into nonferroelectric monoclinic or tetragonal structures. Additionally, increasing thickness beyond the critical nanoscale regime (>10 nm) tends to promote strain relaxation and monoclinic phase formation, thereby degrading ferroelectric properties [8–10].

Another binary material is aluminum nitride (AlN), a well-known third-generation semiconductor material with pyroelectric and piezoelectric properties. It has a wurtzite crystal structure (space group P6_3mc), and spontaneous polarization along the c-axis arises from the asymmetric arrangement of nitrogen and aluminum atoms. However, this spontaneous polarization cannot be switched because the electric field necessary to reverse the polarization (the coercive field) is higher than the electric breakdown field [11]. These limitations could be overcome by doping with suitable elements such as scandium [12]. By introducing Sc into the AlN structure, the piezoelectric coefficient increases [13], the values of the electric breakdown field decrease, and switchable ferroelectric polarization develops [14].

The main challenge in preparing ferroelectric $Al_{1-x}Sc_xN$ thin films is that ScN, which has a rock-salt type ($Fm\bar{3}m$) symmetry (space group #225), and AlN, with the wurtzite-type $P6_3m$ polar space group #176, are immiscible [15]. Therefore, under ambient conditions, solid solutions of AlN and ScN are thermodynamically unstable and might undergo phase segregation, especially at high Sc content (>30%) [16].

The processing complexities make the fabrication of ferroelectric Sc-doped AlN and Zr-doped $HfO_2$ thin films a significant challenge, requiring precise control of composition, crystal structure, stress, defects, and interfaces to achieve reproducible microstructural and electrical performance suitable for device applications. In this chapter, experimental data obtained on $Al_{1-x}Sc_xN$ (ASN) and $Hf_{0.5}Zr_{0.5}O_2$ (HZO) thin films will be presented, with the main aim of establishing correlations among preparation conditions, microstructural features, and electrical properties.

## 2. $Al_{1-x}Sc_xN$ thin films

The $Al_{1-x}Sc_xN$ (ASN) thin films were deposited using radio-frequency (RF) magnetron sputtering with a co-sputtering setup. This is a versatile, effective, and CMOS-friendly method to grow high-quality ASN thin films with tunable electrical properties at relatively low temperatures (below 450°C or even RT) [17, 18]. The substrates used were Pt(111)/Ti/$SiO_2$/Si(100) and TiN/Si(100). The chamber's base pressure was approximately $1 \cdot 10^{-5}$ Pa, and the deposition pressure was 0.22 Pa in a $N_2$-rich reactive atmosphere. Before deposition, the substrates were in-situ Ar plasma cleaned for 5 minutes. The key parameters used for ASN deposition are summarized in **Table 1**.

The microstructure of ASN is essential for achieving the desired electrical properties. The surface morphology of ASN thin films was examined using atomic force microscopy (AFM) in noncontact scanning mode over 5 × 5 μm sample areas (see **Figure 1**). Additionally, the top morphology of ASN thin films deposited by magnetron sputtering was investigated using scanning electron microscopy (SEM) (see **Figure 2**).

From AFM (see **Figure 1**) and SEM images (see **Figure 2**), it is observed that all ASN thin films display well-defined surface grains, low roughness (RMS = 1–2 nm), and uniform surface morphology. The scandium concentration in sputter-deposited films was evaluated using energy dispersive spectroscopy (EDS) analysis, which

| Name | Bottom electrode/ substrate | Thick (nm) | Temp (°C) | Applied power (W) | Atmosphere (sccm Ar: sccm $N_2$) |
|---|---|---|---|---|---|
| ASN405 | Pt/Ti/$SiO_2$/Si (001) | 72 | RT | 100 W – Al<br>60 W – Sc | 22: 6 |
| ASN406 | Pt/Ti/$SiO_2$/Si (001) | 70 | 350 | 100 W – Al<br>60 W – Sc | 22: 6 |
| ASN24P | Pt/Ti/$SiO_2$/Si (001) | 70 | RT | 100 W – Al<br>75 W – Sc | 22: 8 |
| ASN24T | TiN/Si (100) | 70 | RT | 100 W – Al<br>75 W – Sc | 22: 8 |

**Table 1.**
*Deposition parameters of ASN thin films.*

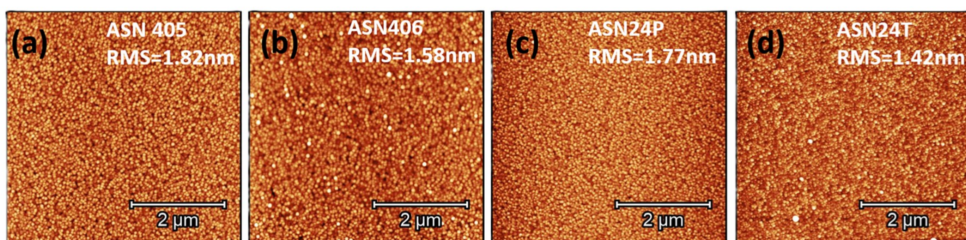


**Figure 1.**
*AFM images of ASN thin films.*

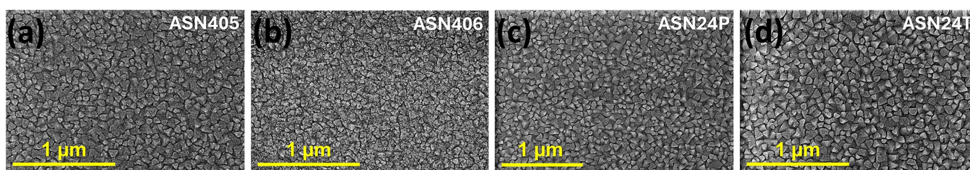


**Figure 2.**
*SEM images of ASN thin films.*

revealed that the film deposited with 22:6 Ar:$N_2$ (21.4% nitrogen ratio) and 60 W on the scandium target has a [Sc/(Sc + Al)] concentration of approximately 15–18%. The wide-range survey spectrum obtained by X-ray photoelectron spectroscopy (XPS) (see **Figure 3a**) confirms the presence of Al, Sc, N, O, and surface contaminants, such as carbon. High-resolution spectra of the Al 2p, C 1s, Sc 2p, N 1s, and O 1s core levels (see **Figure 3b–3i**) were analyzed to identify specific chemical states and quantify the corresponding bonding configurations.

Quantification from the high-resolution spectra (see **Figure 3b–3i**) shows the atomic concentrations at the top surface of ASN thin films deposited at RT (ASN405) or at 350°C (ASN406) – see **Table 2**.

These values correspond to a cationic scandium fraction: Sc/(Sc + Al) ~ 0.10 for ASN 405 (approximately 10 at.% Sc at the ASN surface) and approximately 0.09 for ASN 406 (~9 at.% Sc at the ASN surface, in terms of cationic concentration). The scandium percentage values derived from the XPS analysis are significantly lower than the bulk concentration measured by EDS. This difference results from the markedly different probing depths of the two techniques: Energy dispersive spectroscopy analyzes material on the micrometer scale, while XPS is sensitive only to the top ~ 3–5 nm of the surface.

An obvious observation is the surface depletion of scandium, which is linked to its tendency to oxidize. This results in more Sc–O bond formation compared to Sc–N bonds (see **Table 3**). Several groups have already reported this phenomenon [19, 20]. An aspect worth noting is that the ASN layer deposited at 350 °C is more stable against oxidation than the film grown at RT. The Al 2p region is fitted with two components (Comp1 and Comp2): one corresponding to Al – N (~73 eV) and another to the oxidation product Al – O (~74 eV). Room temperature-deposited samples (ASN405) show an Al – O component of 25.57%, with the dominant Al–N at 74.43%, while ASN406 (deposited at 350 °C) exhibits a lower fraction of oxidized Al

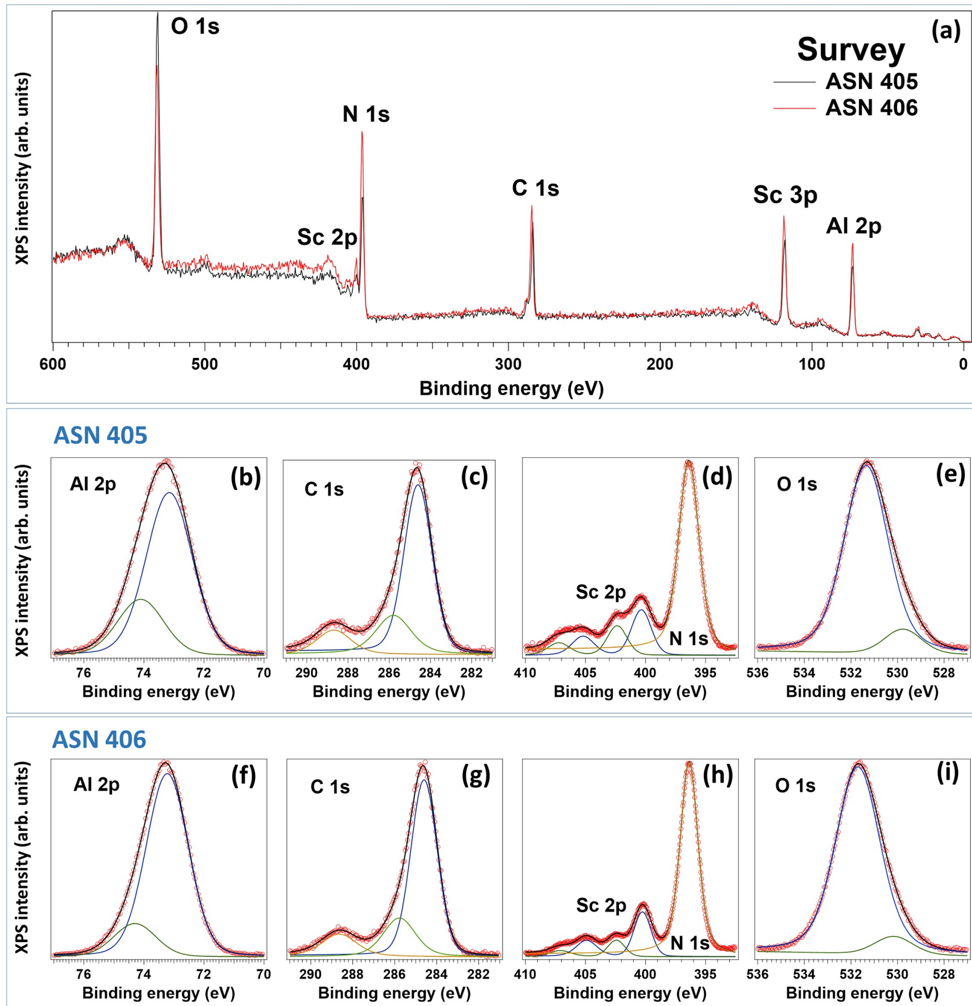


**Figure 3.**
*(a) X-ray photoelectron spectroscopy (XPS) survey spectrum of the ASN405 and ASN406 thin films. High-resolution spectra of Al 2p for (b) ASN405 and (f) ASN406 are deconvoluted into Al–N and Al–O components; C 1s for (c) ASN405 and (g) ASN406; the combined Sc 2p/N 1s region of (d) ASN405 and (h) ASN406, with Sc 2p deconvoluted into Sc–N and Sc–O; and O 1s for (e) ASN405 and (i) ASN406 showing oxygen-containing surface species associated with Al–O and Sc–O bonds.*

| ASN405 | | ASN406 | |
|---|---|---|---|
| O | 36.0 | O | 24.7 |
| Al | 37.4 | Al | 42.7 |
| Sc | 4.2 | Sc | 4.2 |
| N | 22.3 | N | 28.4 |

**Table 2.**
*Atomic concentration (%) of elements detected by XPS in ASN405 and ASN406.*

| ASN 405 | Al | | Sc | |
|---|---|---|---|---|
| | Comp1 | Comp2 | Comp1 | Comp2 |
| BE (eV) | 73.02 | 73.97 | 400.34 | 402.36 |
| I(cps) | 8768.84 | 3012.22 | 811.63 | 526.29 |
| C(%) | 74.43 | 25.57 | 60.66 | 39.34 |
| **ASN 405** | | | | |
| BE (eV) | 73.09 | 74.17 | 400.25 | 402.42 |
| I(cps) | 12741.38 | 2305.62 | 1092.75 | 403.70 |
| C(%) | 84.68 | 15.32 | 73.02 | 26.98 |
| Attribution | Al–N | Al–O | Sc–N | Sc–O |

**Table 3.**
*Al 2p and Sc 2p deconvolution results for nitride and oxide components of ASN405 and ASN406 layers.*

(Al – O at 15.32%). The scandium components (Sc–N at ~ 402.3 eV and Sc–O at ~ 402.4 eV) display the same trend of lower oxidation at higher temperature, but with more significant values for Sc–O fractions (~39.34% for ASN405 and 36.98% for ASN406).

To achieve ferroelectricity, the scandium concentration should be higher, according to scientific literature [16, 21]. The optimal scandium concentration [Sc/(Sc + Al)] that reduces the energy barrier between the two polarization states of the wurtzite structure and enables ferroelectric switching is ~ 22–30%.

The straightforward way to increase the Sc content is to increase the power applied to the scandium target. In fact, by increasing the power from 60 W to 75 W, EDS analysis shows that the scandium concentration increased to ~ 30%, indicating a composition consistent with $Al_{0.7}Sc_{0.3}N$. The ratio of working gas to reactive gas mixture was adjusted to 22 sccm Ar and 8 sccm $N_2$. For this gas mixture, the sputtering should be in a sensitive state, close to the boundary between metallic and poisoned regimes, but leaning toward poison mode. This mode is known to enable ferroelectric switching in sputtered Al–Sc nitrides and to reduce leakage currents, which are one of the main causes of electrical breakdown. The difficulty of producing a purely wurtzite phase, especially at high scandium content, increases the complexity of obtaining ferroelectric ASN layers.

To gain a deeper understanding of the microstructure of the ASN thin film, TEM and high-resolution transmission electron microscopy (HRTEM) experiments were conducted. The TEM analysis of the ASN406 sample and the corresponding SAED pattern are shown in **Figure 4**. From **Figure 4b**, it is observed that a set of diffraction spots appears from the central transmitted beam, which can be attributed to the ASN thin film. Measurements of the SAED pattern revealed four distinct sets of diffraction spots, which were indexed and assigned their respective Miller indices. The ASN thin film crystallizes in a hexagonal wurtzite structure with lattice parameters a = b = 0.308 nm and c = 0.503 nm.

The elongation of diffraction spots along the (0001) direction, combined with the presence of extra reflections forbidden by the structure factors, such as the (0001) reflection, strongly suggests a columnar growth mode. This indicates that the ASN film mainly consists of structural domains separated by planar defects, likely at the interfaces between columns.

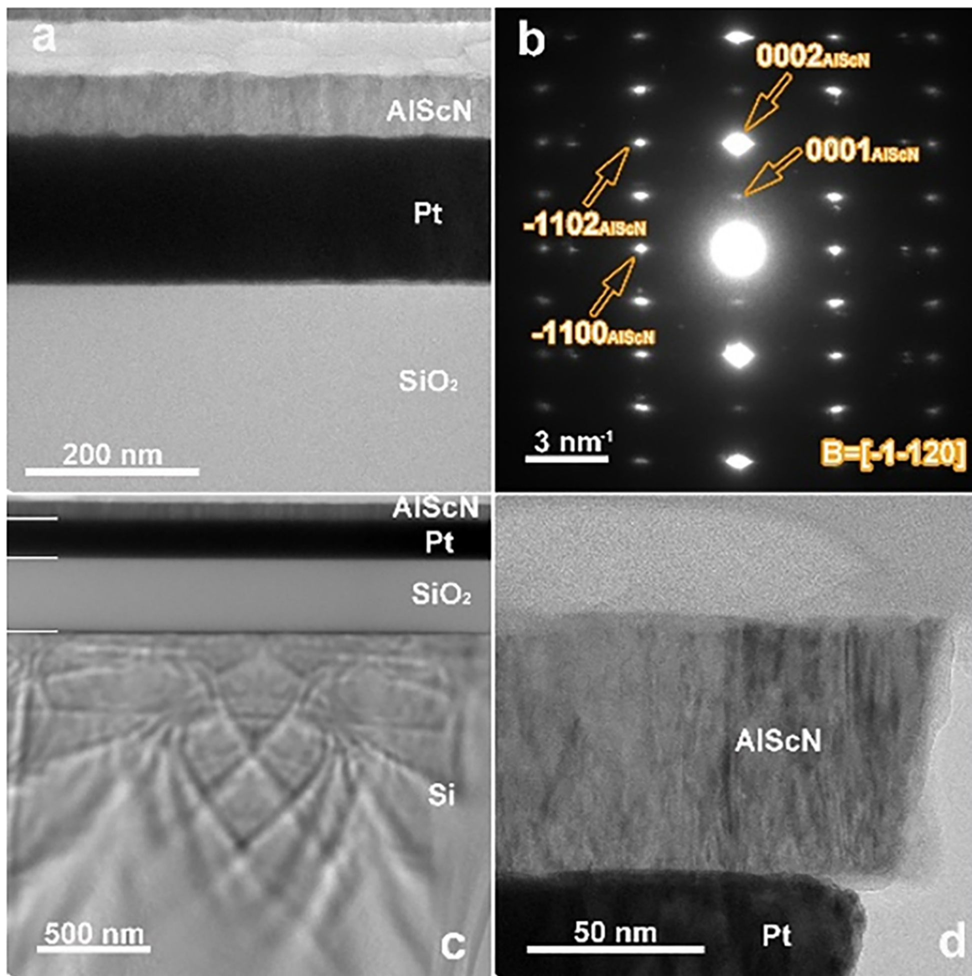


**Figure 4.**
*(a) Cross-section TEM image at low magnification showing the ASN/Pt/$SiO_2$ heterostructure, (b) SAED pattern corresponding to the TEM image in (a), (c) cross-section TEM image of the ASN/Pt/$SiO_2$/Si heterostructure, and (d) TEM image recorded at the interface between ASN and Pt.*

The low-magnification TEM images in **Figure 4c,d** display the entire cross-section of the sample, including all deposited layers.

A representative HRTEM micrograph is shown in **Figure 5a**. Close inspection reveals a columnar growth mode for the ASN film, with domains showing lateral relaxation over several tens of nanometers. This is further illustrated in **Figure 5b**, where three distinct domains are marked as regions 1, 2, and 3. High-resolution transmission electron microscopy measurements on the domain labeled as region 1 show well-resolved lattice fringes, with an interplanar spacing of 0.2501 nm. This spacing corresponds to the (0002) lattice planes, confirming the hexagonal wurtzite structure of the ASN thin film.

The columnar growth is also supported by the fast Fourier transform (FFT) analysis shown in **Figure 5d**, which corresponds to the HRTEM image in **Figure 5a**. In the FFT pattern, an elongation of diffraction spots along the [0001] direction can be observed, consistent with the presence of columnar domains and associated planar defects.

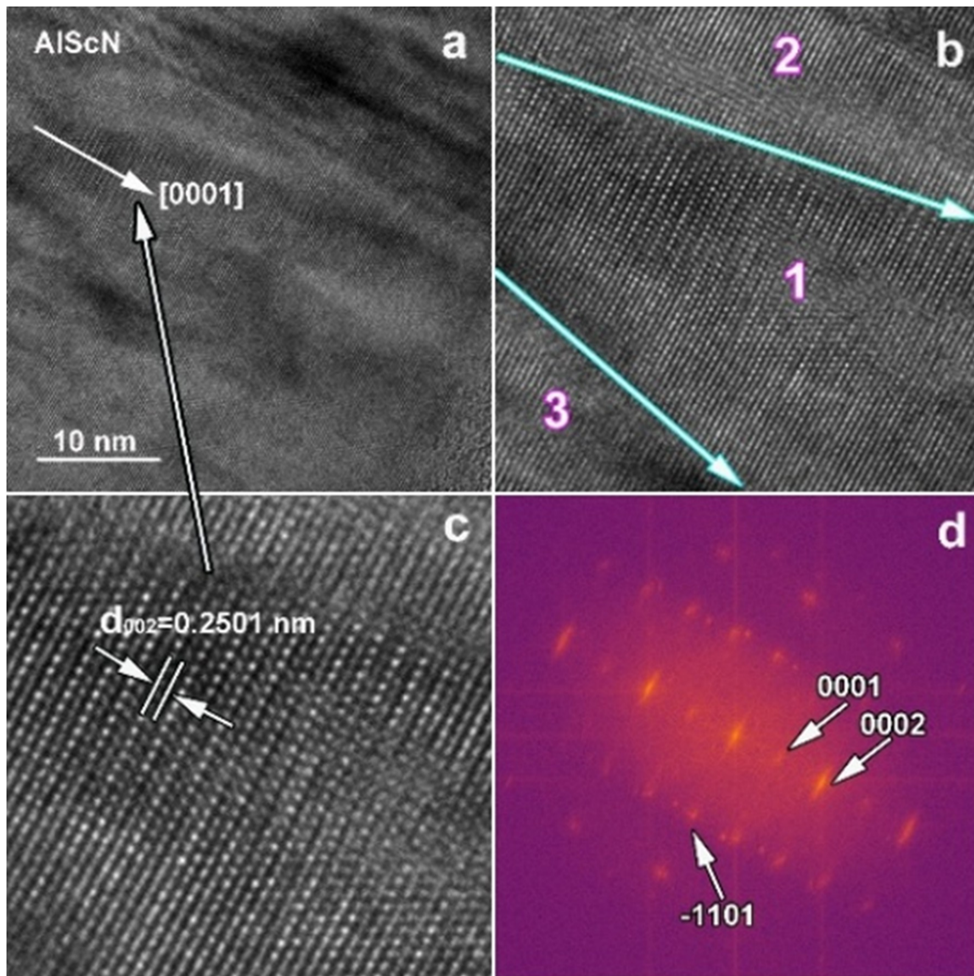


**Figure 5.**
*(a) HRTEM image of the ASN thin film taken along the [0001] direction, (b) and (c) magnified views of the ASN lattice fringes, and (d) FFT pattern corresponding to the entire HRTEM image in (a).*

## 2.1 Electrical properties of ASN films

The electrical investigations of these samples focused on their ferroelectric properties. For these measurements, the AlScN thin films were integrated into capacitor structures by depositing platinum top electrodes with circular shapes using photolithography, lift-off, and sputtering. The electrical measurements were conducted at RT on the AlScN samples and are shown in **Figure 6**. For samples deposited on Pt, those prepared at RT with different scandium concentrations, ASN405 and ASN24P, showed very similar ferroelectric behaviors. As observed from the current–voltage (I–V) curves related to the polarization curves, there is a general increase in current for the sample deposited with higher power applied to the Sc target, resulting in polarization curves inflated with abnormally high values compared to the typical ~100 $\mu C/cm^2$ reported for this material [22, 23]. The increase is due to the high leakage currents at elevated voltages. When the substrate

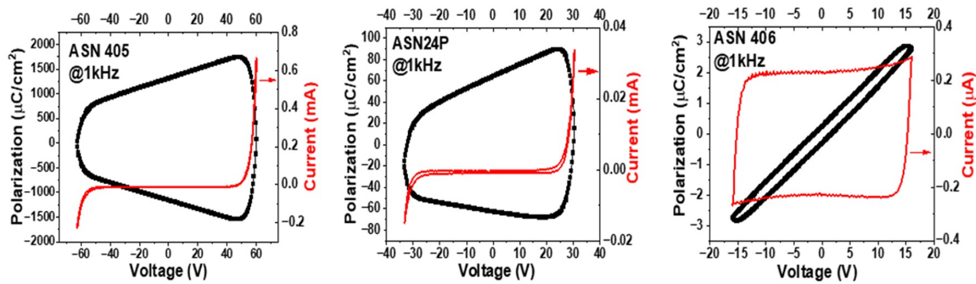


**Figure 6.**
*Electrical characteristics of the Pt/ASN/Pt samples.*

temperature was raised to 350°C, the ASN406 sample's I–V curve resembled that of a dielectric material. From the hysteresis measurements performed on ASN406, it is difficult to determine if this sample is ferroelectric because the applied electric field was lower than the reported coercive field (~5 MV/cm) [24]. For the studied ASN films, at a thickness of 70 nm, the coercive voltage should be around 35 V. Based on ASN's bandgap, the intrinsic breakdown field is at least two times higher than the coercive field. However, the breakdown field for samples deposited on Pt was 60 V for ASN405, 33 V for ASN24P, and 15 V for ASN406, which were lower than the estimated values. No current peaks associated with ferroelectric switching were observed in any of the samples deposited on Pt.

The appearance of electrical breakdown at values lower than the intrinsic breakdown field has been reported in the literature and was attributed to defects in the film [25, 26], which, in our case, can be linked to differences in stoichiometry and microstructure between the surface and the bulk of the film. An important factor influencing electrical properties is the choice of electrode materials. At the interface between the electrode and the ASN film, the electrical properties differ from those in the bulk. For example, in samples with Pt electrodes, the work function of Pt is around 5.6 eV to 6.35 eV [27], which is higher than the band gap of the ASN films [28]. Due to this difference, this type of electrode injects electrons into the ASN films more easily, and the local field at the Pt/ASN interface can be much higher than the applied field, leading to electrical breakdown before other phenomena, such as ferroelectric switching. Another option for electrodes is TiN, which is commonly used in microelectronic applications. TiN is nitrogen-stable, compatible with CMOS technology, and forms a chemically inert interface with the ASN film. It has a lower work function of about 3.4 eV [29] than Pt, which limits electron injection and results in a more stable electrical contact with the ASN films.

**Figure 7** shows the results of hysteresis measurements performed on ASN thin films deposited on TiN (ASN24T sample). In the initial I–V curve measurements related to polarization, two distorted peaks are observed in both positive and negative voltage ranges. Upon repeating the measurements, the hysteresis data reveal only one peak current in the I–V curve within the negative voltage range, followed by a linear increase in the positive voltage range. The peak position and amplitude vary with the test signal's frequency (see **Figure** 7), similar to the behavior seen in ferroelectric materials.

This current peak is also evident in PUND measurements. These measurements show that the peak current appears in both I–V curves recorded after applying Pulse

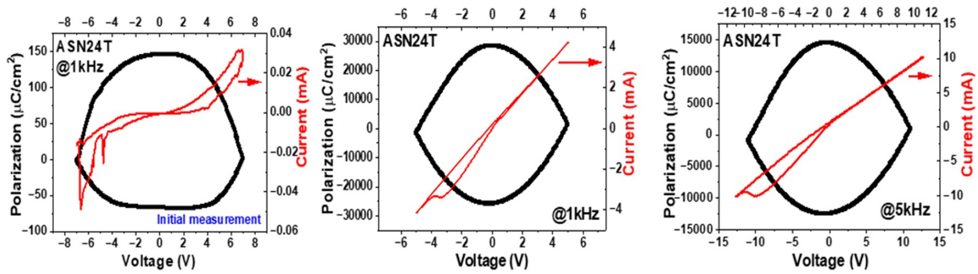


**Figure 7.**
*Ferroelectric hysteresis measurements performed at 1 kHz and 5 kHz for the sample deposited on TiN/Si.*

1 (the switching pulse) and Pulse 2 (the so-called nonswitching pulse). The peak gradually diminishes as the delay time between Pulse 1 and Pulse 2 decreases (see **Figure 8**). This behavior is common in ferroelectric thin-film materials with a preferential ferroelectric orientation and is typically attributed to ferroelectric polarization back-switching.

This current peak only appears when the sample is tested with triangular signals. No current peak is observed for DC voltage (see **Figure 9**).

A notable feature of this current peak is that its position can be reversibly adjusted by changing the voltage in the positive voltage range (see **Figure 10**). This effect is more evident when the delay time ($t_R$) between the positive and negative voltage pulses is $10^{-4}$ seconds. The fact that the shape of the I–U curve is reversible and reverts to its original form when the positive voltage value is decreased indicates a memory effect.

One possible explanation is the presence of ferroelectric switching on the positive voltage, which is not visible with the PUND and dynamic hysteresis methods due to leakage current. In this case, the changes observed in the current peak amplitude and position could be attributed to contributions from ferroelectric domains that were partially switched with the positive voltage pulse. However, the fact that this current peak is only visible after the voltage was cycled through the sample at 8 V and the dielectric impedance decreased by about two orders of magnitude (from 530 kΩ before voltage cycling to 986 Ω at 60 kHz) suggests that other phenomena, such as resistive switching, could be responsible for the observed memory effect. The similarity of the I–V curves (see **Figure 9c**) measured on electrodes with different areas indicates that resistive switching is filamentary [30–32]. In filamentary resistive switching, conductive paths form and rupture within the layer, so the current does not scale proportionally with electrode area as it would for homogeneous conduction. This implies that the electrode material type and the resulting interface properties are important in modulating the functional behavior of ASN thin films.

## 3. HZO thin films

Ferroelectricity in hafnium–zirconium oxide ($Hf_{0.5}Zr_{0.5}O_2$, HZO) has gained significant interest recently due to its compatibility with CMOS technology and its remarkable ferroelectric stability at nanometer-scale thicknesses. Unlike traditional perovskite ferroelectrics, HZO exhibits a metastable polar orthorhombic phase whose stabilization depends heavily on factors such as film thickness, growth

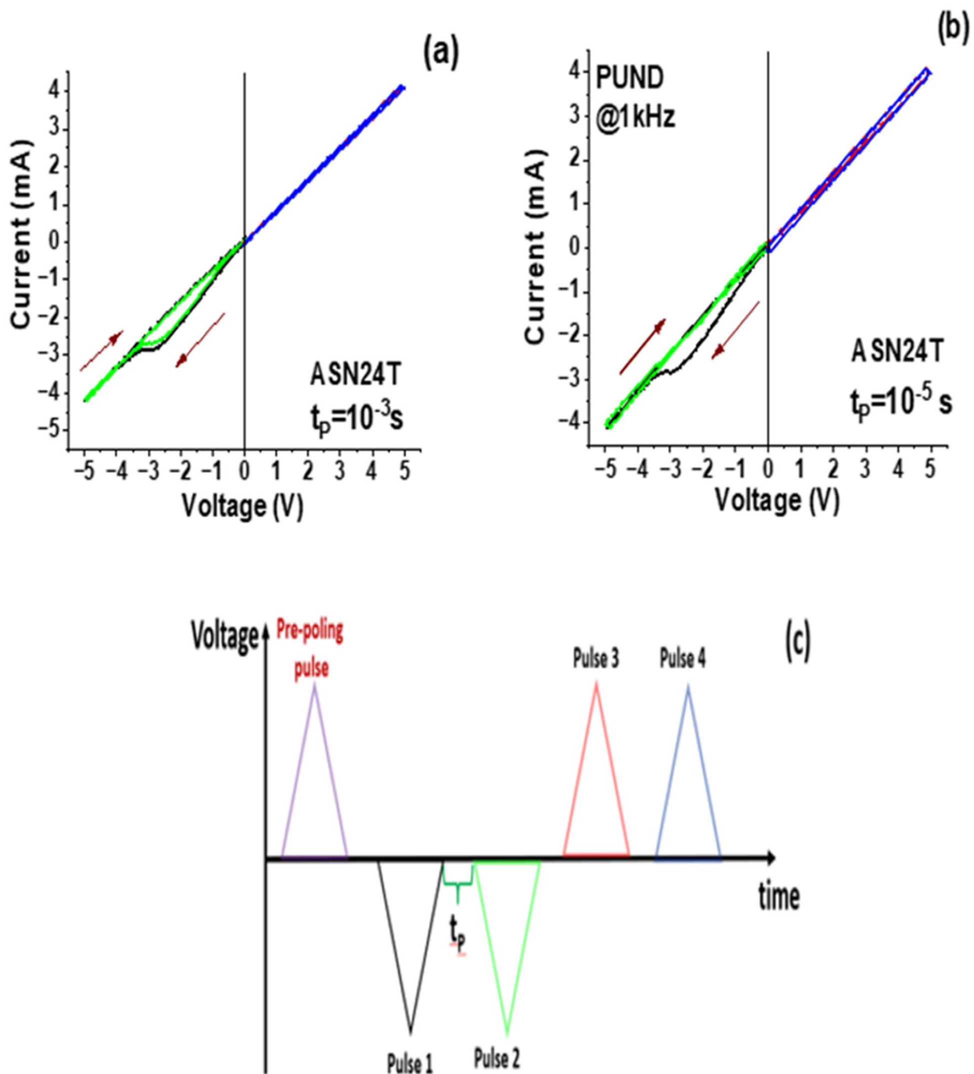


**Figure 8.**
*(a, b) Current–voltage curves measured by the PUND method on ASN24T at different delay times ($t_p$) between Pulse 1, Pulse 2, Pulse 3, and Pulse 4, and (c) pulse sequence used during the PUND measurements.*

conditions, epitaxial strain, and the nature of the bottom electrode. In epitaxial heterostructures, the bottom electrode's influence is especially important, as it can affect both the structural nucleation and the electrical properties of the ferroelectric film. In this context, $La_{0.67}Sr_{0.33}MnO_3$ (LSMO) is a promising bottom electrode material because of its high electrical conductivity, structural compatibility with $SrTiO_3$ (STO), and ability to grow epitaxially via the pulsed laser deposition (PLD) method. However, the structural and electrical properties of LSMO are strongly thickness-dependent [33]. Ultrathin LSMO films may exhibit degraded interfacial properties, increased resistivity, and the so-called dead-layer effects, while thicker films tend to behave more like bulk material, displaying improved conductivity and

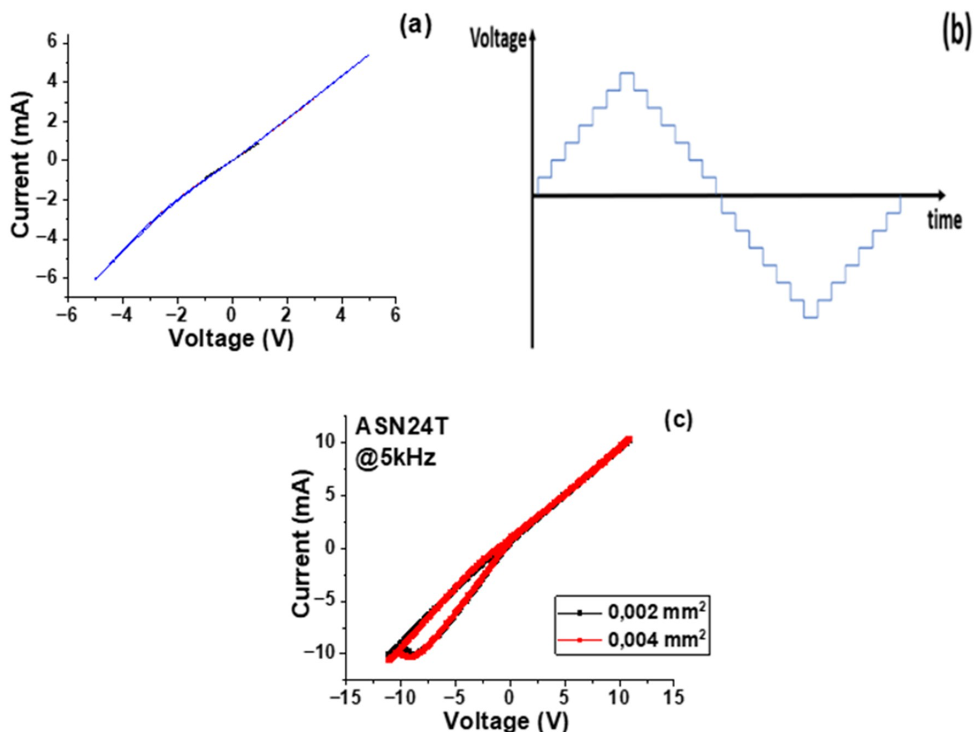


**Figure 9.**
*(a) Current–voltage measurements obtained by applying DC voltage; (b) pulse sequence used during the measurements; and (c) comparison of current–voltage curves measured with top electrodes of different areas.*

structural stability. In this study, we investigate how the thickness of the LSMO bottom electrode affects the structural growth and phase composition of epitaxial HZO thin films deposited on STO substrates by PLD. Two heterostructures were compared: STO/LSMO(40 nm)/HZO and STO/LSMO(20 nm)/HZO, with all other deposition parameters held constant. The nanoscale structural properties were analyzed using TEM and HRTEM, focusing on how the structural state of LSMO relates to the nucleation, orientation, and phase distribution of HZO.

The HZO thin films were deposited on single-crystalline STO (001) substrates supplied by CrysTec GmbH. These substrates had a miscut angle ranging from 0.05° to 0.5°. Before depositing the HZO films, preliminary substrate preparation was performed. This involved transforming the optically polished surface into one with steps and terraces that are highly organized at the atomic level (see **Figure 11**). To achieve this, the STO substrates were etched in an $NH_4$-HF solution for 15 seconds to remove any Sr residues. Afterward, the substrates underwent thermal treatment at ~1000°C for 4 hours.

The deposition of the HZO films was performed using an in-house target with a 50/50 composition ratio, along with a commercial $La_{1-x}Sr_xMnO_3$ (x = 0.33) (LSMO) target with a 0.67/0.33 ratio from Praxair. For the LSMO layer, deposition was conducted at a substrate temperature of 800 °C, with a laser fluence of 1 J/cm$^2$ and a repetition rate of 5 Hz. The deposition process took place in an oxygen atmosphere, with the partial pressure maintained at 0.1 mbar. The HZO films were deposited at

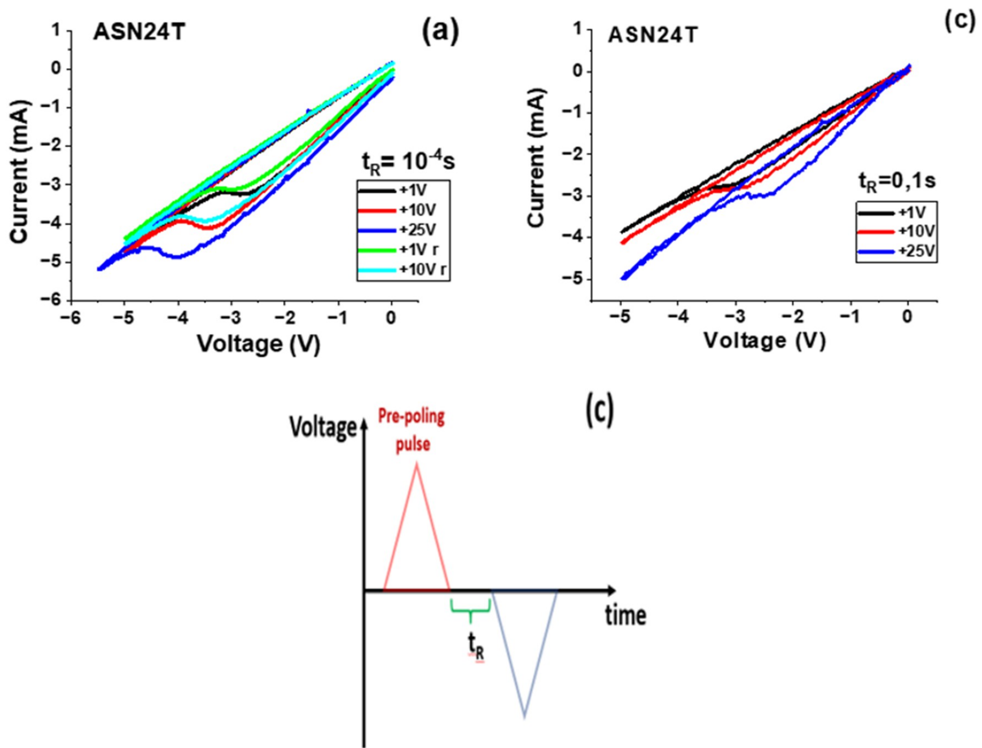


**Figure 10.**
*(a, b) Current–voltage curves obtained for various delay time values ($t_r$) between the positive and negative pulses, and (c) graphical representation of the pulse sequence applied during the measurements.*

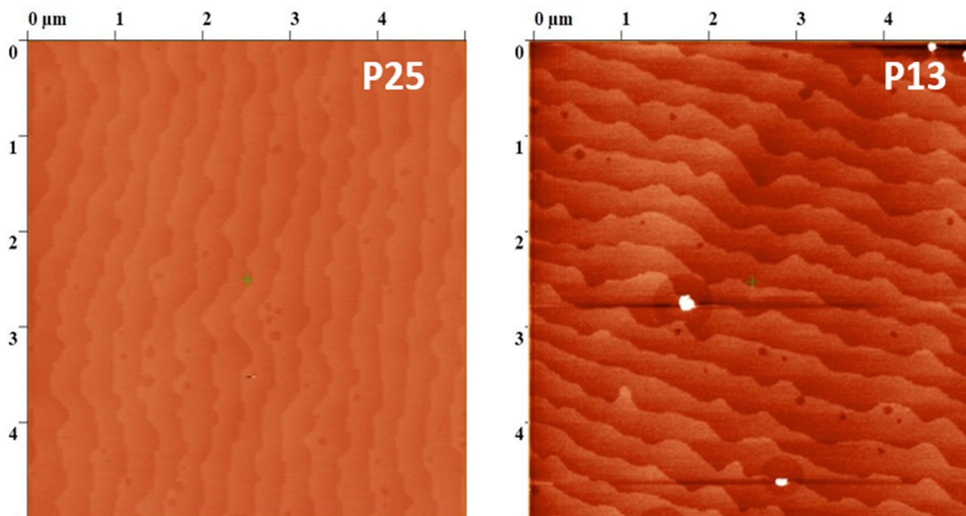


**Figure 11.**
*Atomic force microscopy images of STO (001) substrates after chemical etching and thermal treatment.*

the same substrate temperature of 800 °C using a laser fluence of 1.1 J/cm$^2$ and a repetition rate of 2 Hz. During deposition, the oxygen partial pressure was consistently kept at 0.1 mbar for all samples. The number of laser pulses applied for the LSMO layer was 2500 for the P13 sample and 1565 for the P25 sample. Immediately following the HZO deposition, the substrate temperature was maintained at 800 °C while oxygen was introduced at maximum flow rate until reaching a pressure of 0.2 mbar. The sample was then cooled down to RT without a ramp-down procedure.

The symmetric 2θ-ω XRD scans, shown in **Figure 12**, were performed at RT on a Rigaku SmartLab diffractometer set to high-resolution mode using an X-ray mirror and a two-bounce Ge (400) monochromator. These scans reveal a strong crystallographic similarity between both films. The sample's cut-off was aligned according to the substrate's STO (002) orientation. In the 2θ = 18–37° region, 2θ-ω patterns were measured at a speed of 1 gpm with a step size of 0.02. The XRD data of both samples indicate that in HZO, the orthorhombic phase is dominant (P21/c – PDF 04-002-5428). The XRD pattern exhibits well-defined thickness fringes around the main LSMO (00 l) diffraction peak. The presence of these oscillations indicates that the 20 nm LSMO film is highly epitaxial, structurally coherent, and smooth at the interfaces, with a well-defined and uniform thickness. These fringes also suggest that the film remains more strained and elastically coupled to the STO substrate, as thinner epitaxial films tend to retain the lattice mismatch–induced strain rather than relax through defect formation. In contrast, for sample P13 (HZO deposited on LSMO = 40 nm), the LSMO (00 l) peak is still clearly present and sharp, confirming good crystallinity, but the thickness fringes are no longer visible. This is not interpreted as a loss of epitaxy but rather as a consequence of partial strain relaxation at larger thicknesses. At around 40 nm, LSMO is expected to accommodate mismatch strain via the formation of misfit dislocations or other relaxation mechanisms, which broaden the diffraction features and suppress interference fringes. Thus, the disappearance of fringes in P13 is consistent with a more relaxed, bulk-like structural state of the LSMO film. Regarding the HZO layer, distinct diffraction peaks corresponding to specific monoclinic or orthorhombic reflections are not clearly resolved in the XRD

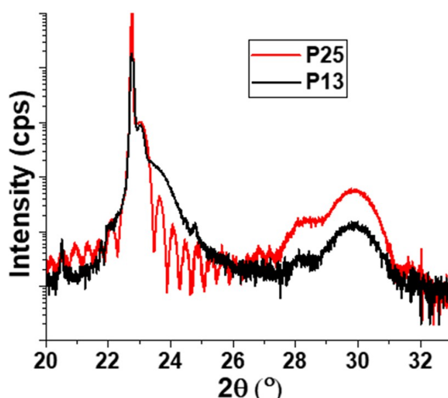


**Figure 12.**
*High-resolution θ–2θ XRD scans of the LSMO (00 l) reflection for HZO/LSMO/STO heterostructures with 40 nm (P13) and 20 nm (P25) LSMO bottom electrodes.*

patterns due to its ultrathin ~ 8 nm thickness and nanocrystalline nature. Therefore, the detailed phase identification of HZO relies primarily on HRTEM and FFT analysis rather than on XRD. It is also important to consider the TEM observations in light of the XRD results. Although localized amorphous regions were detected in the 20 nm LSMO layer from the P25 sample by HRTEM, the presence of clear fringes in XRD strongly suggests that the as-deposited LSMO film was originally epitaxial and structurally coherent. Consequently, the local amorphization observed in TEM is likely at least partly induced by the ion-milling and thinning process used to prepare the cross-sectional lamella, rather than being an intrinsic feature of the film grown by PLD. The more strained and coherent state of the 20 nm LSMO film likely modifies the local interfacial environment during HZO nucleation, which may contribute to the observed differences in grain size, texture, and phase distribution compared to the more relaxed 40 nm LSMO electrode.

Cross-sectional low-magnification TEM of P13 (see **Figure 13a**) shows a continuous multilayer stack with an ~ 8 nm HZO film on a ~ 40 nm LSMO electrode. The layers are uniform, and the HZO/LSMO interface appears continuous over large areas. The corresponding SAED pattern (see **Figure 13b**) taken from a region including STO, LSMO, and HZO, exhibits strong STO reflections; LSMO reflections overlap with STO due to their close pseudocubic lattice match. Additional diffraction features related to HZO display an elongated character consistent with a small distribution of orientations (≈ ± 5°), indicating that HZO domains are slightly tilted relative to the surface normal. High-resolution transmission electron microscopy images across the HZO/LSMO interface (see **Figure 14a**) reveal locally oriented HZO regions. Lattice-fringe analysis combined with FFT/inverse fast Fourier transform (IFFT) filtering

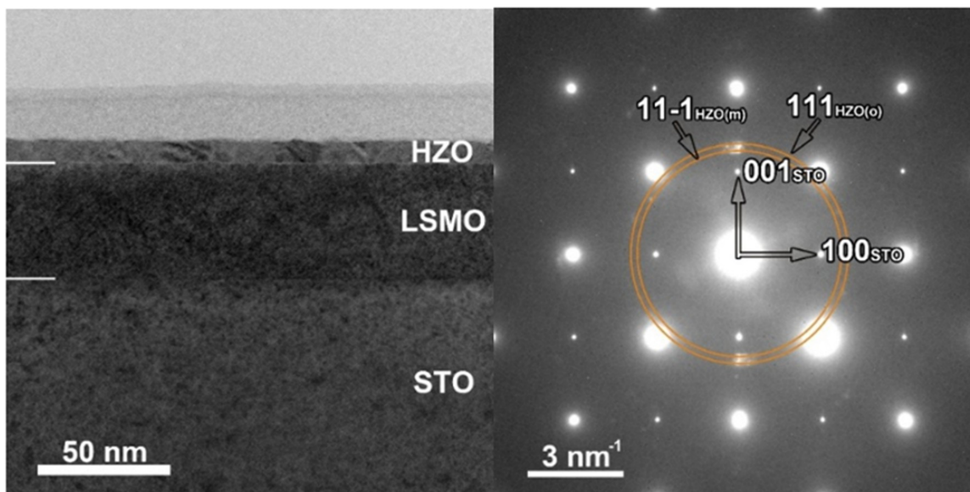


**Figure 13.**
*(a) Low-magnification cross-sectional TEM image of sample P13 (STO/LSMO 40 nm/HZO), showing a continuous multilayer stack with a uniform HZO thickness (~8 nm). (b) Corresponding SAED pattern taken from a region including STO, LSMO, and HZO; strong STO reflections are visible, while HZO diffraction features appear elongated, indicating a slight tilt (±5°) of HZO domains relative to the surface normal and a mixed monoclinic/orthorhombic phase character.*

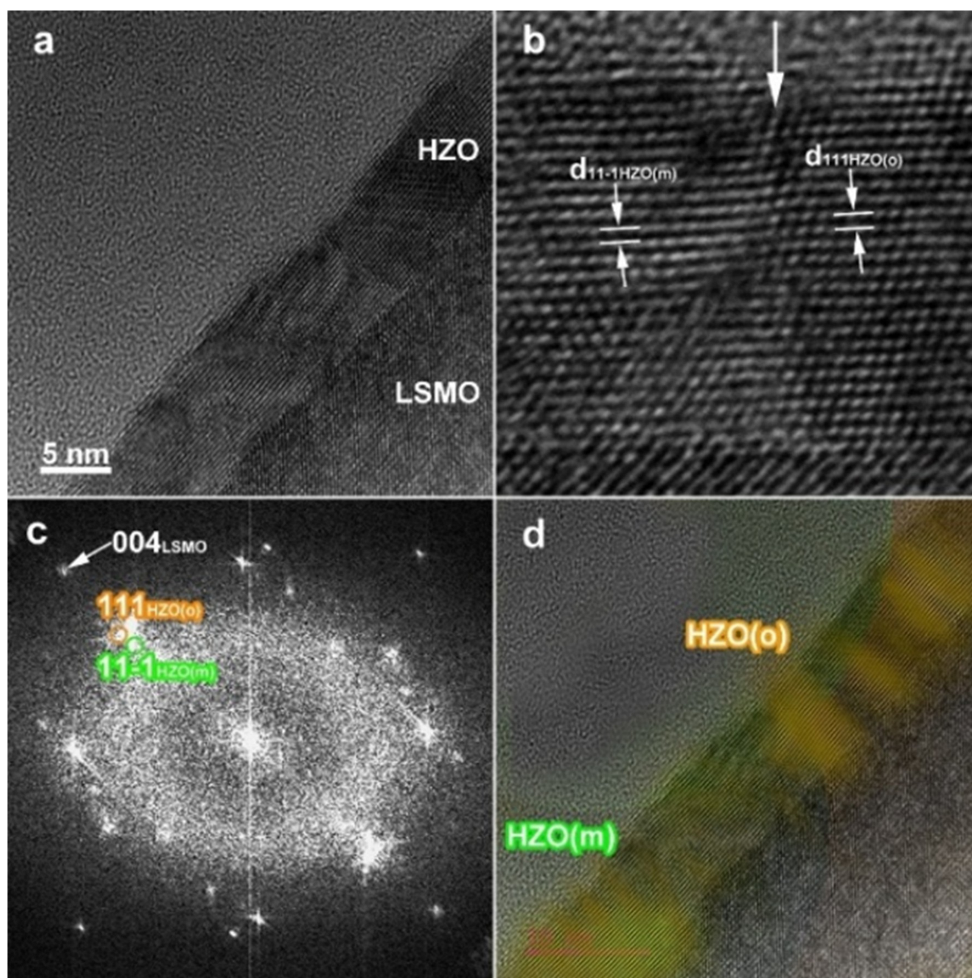


**Figure 14.**
*(a) HRTEM image recorded at the HZO/LSMO interface, (b) detail extracted from the HRTEM image showing the (11–1)HZO(m) and (111)HZO(o) lattice fringes rotated relative to the surface normal, (c) FFT pattern corresponding to the HRTEM image (a), and (d) inverse Fourier transform image obtained by filtering the (11–1)HZO(m) and (111)HZO(o) peaks from the FFT pattern and overlapped over the HRTEM image to illustrate the spatial distribution of the HZO monoclinic and orthorhombic crystalline phases.*

(see **Figure 14b–d**) shows a mixture of monoclinic and orthorhombic HZO domains, with the (11–1)(m) spacing (~0.312 nm) and (111)(o) spacing (~0.296 nm) identified in adjacent regions. The reconstructed IFFT phase map (see **Figure 14d**) highlights the spatial distribution of monoclinic and orthorhombic regions and confirms the coexistence of mixed phases at the nanoscale.

Interpreted together with XRD (see **Figure 12**), the more relaxed state of the 40 nm LSMO electrode likely creates a less strained interfacial boundary condition for HZO nucleation and cooling, thereby promoting the development of the thermodynamically stable monoclinic phase alongside the metastable orthorhombic phase.

*DOI: http://dx.doi.org/10.5772/intechopen.1015311*

For P25, low-magnification TEM (see **Figure 15a**) confirms a similar HZO thickness (~8 nm) grown on a thinner (~20 nm) LSMO electrode. The multilayer stack remains continuous and aligned with the STO substrate.

The SAED pattern (see **Figure 15b**) shows strong STO reflections and faint HZO rings, indicating a nanocrystalline film. Several HZO regions display partial alignment with the electron beam in HRTEM (see **Figure 16a**). In the three analyzed areas (A1–A3 in **Figure 16a**), one region shows a spacing consistent with monoclinic HZO (~0.314 nm for (11–1)(m)), while the other areas exhibit intermediate values between monoclinic and orthorhombic spacings (see **Figure 16b–d**). This indicates a heterogeneous nanoscale mixture and/or a nonequilibrium transformation pathway during cooling.

A particularly strong structural finding in P25 is the identification of zone axis–oriented grains whose FFT can be consistently indexed with orthorhombic HZO ($Pca2_1$). As shown in **Figure 16b–d**, the FFT from a single grain (orange circle in **Figure 16a**) exhibits characteristic orthorhombic reflections, including the {111} family and the (002)(o) planes.

For the LSMO layer, which has a pseudocubic structure with a unit cell doubled along the c-axis (c = 0.779 nm), the (002)LSMO peak overlaps with the (001)STO peak due to STO's smaller lattice parameter (c = 0.389 nm), which is nearly equal to the distance between the (002) lattice planes of LSMO, d002 = 0.3895 nm. To avoid overcrowding in the SAED pattern, the LSMO peaks were omitted. Additionally, two concentric circles of faint diffraction spots can be observed, attributed to the (111) planes of HZO in both orthorhombic and monoclinic phases. These correspond to interplanar spacings of 0.296 nm in the orthorhombic phase and 0.283 nm in the monoclinic phase. This confirms the polycrystalline nature of the HZO thin film.

FFT analysis over larger regions (see **Figure 17c**) reveals the simultaneous presence of monoclinic (11–1)(m) and orthorhombic (002)(o) contributions. An IFFT reconstruction based on these reflections (see **Figure 17e**) highlights adjacent

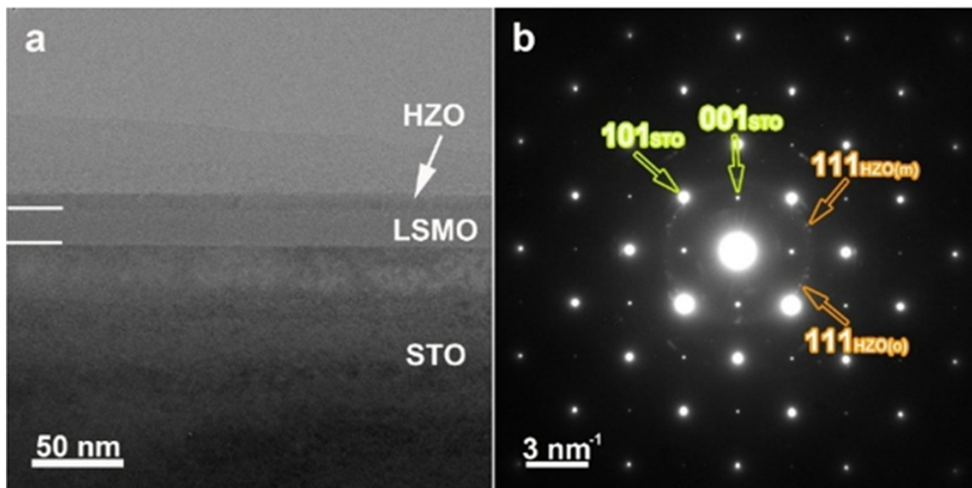


**Figure 15.**
*(a) Low-magnification cross-sectional TEM image of sample P25 (STO/LSMO 20 nm/HZO), revealing a continuous stack with an HZO thickness of ~ 8 nm and an LSMO thickness of ~ 20 nm. (b) SAED pattern from the multilayer region displaying strong STO reflections and faint HZO rings consistent with a nanocrystalline film.*

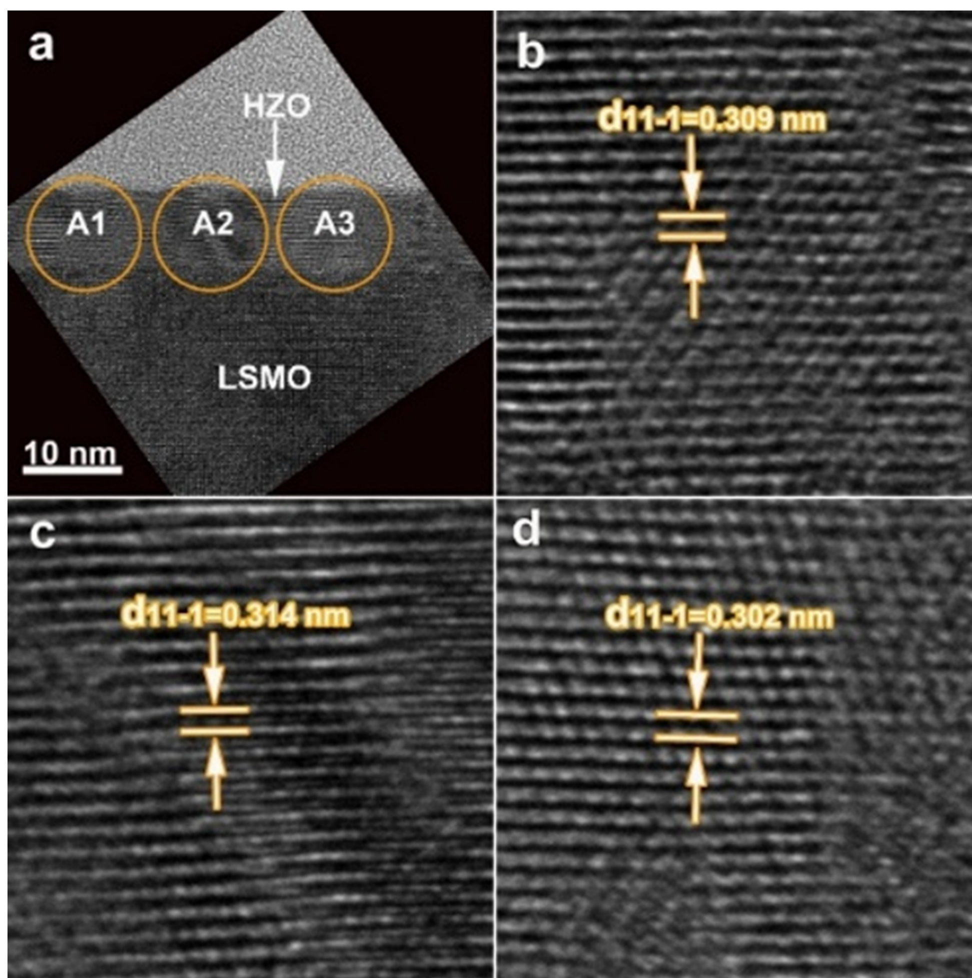


**Figure 16.**
*(a) HRTEM image of the 8-nm-thick HZO deposited on the LSMO electrode; three oriented HZO regions are marked in the HRTEM image. (b–d) Magnified views of the three oriented HZO areas, showing the (111) textured growth of the HZO thin film.*

monoclinic and orthorhombic grains with a local misorientation of approximately 5°, as further illustrated by the atomic structural models in **Figure 17f**. High-resolution transmission electron microscopy shows that in some localized regions of the TEM lamella, the LSMO appears amorphous (see **Figure 16a**), while in other regions, it remains crystalline. However, the clear interference fringes observed in XRD for the 20 nm LSMO film (see **Figure 12**) provide strong evidence that the as-grown LSMO layer was epitaxial, smooth, and structurally coherent.

Therefore, the local amorphization observed in TEM is likely partly caused by TEM specimen preparation, especially during ion milling and final thinning of the lamella. This interpretation is supported by the fact that amorphous regions mainly appear in the thinnest and most damaged parts of the lamella. Importantly, even in these damaged regions of LSMO, the HZO film remains crystalline (see **Figure 16a,b**), showing strong crystallization of HZO under the employed PLD conditions.

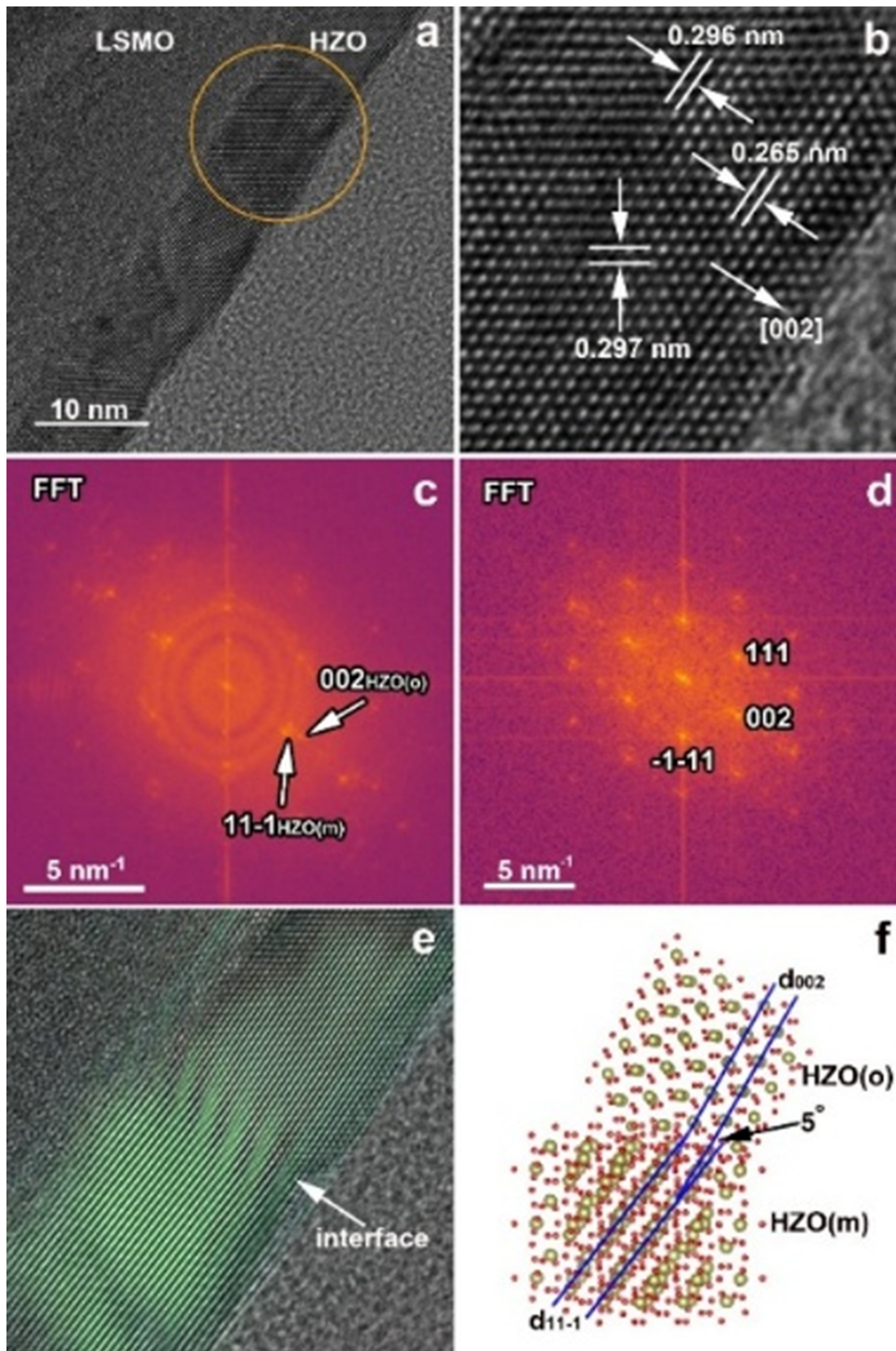


**Figure 17.**
*(a) HRTEM image of a zone axis–oriented HZO grain grown on locally damaged (apparently amorphous) LSMO in sample P25. (b) Magnified image of the selected grain HRTEM image of adjacent HZO grains in sample P25. (c) Corresponding FFT from a larger area showing simultaneous monoclinic (11–1)(m) and orthorhombic (002)(o) reflections. (c,d) IFFT reconstruction highlighting the spatial distribution of monoclinic and orthorhombic grains. (f) simulated atomic structural models (zone axis [1-10]) illustrating the ~ 5° mis-orientation between the out-of-plane directions of orthorhombic (002) and monoclinic (11–1) planes at the phase boundary. For clearer visualization, the interface was simulated using VESTA.*

The combined XRD + TEM data support the idea that the main “global” difference between the two stacks is the strain or coherence state of the LSMO electrode (coherent/strained at 20 nm vs. more relaxed at 40 nm). This difference can alter the interfacial boundary conditions during HZO nucleation and cooling, possibly shifting the balance between orthorhombic (metastable, ferroelectric) and monoclinic (stable) polymorphs, and affecting texture and grain morphology.

### 3.1 Comparative interfacial analysis of P13 and P25

A closer side-by-side examination of the HZO/LSMO interface uncovers subtle yet consistent differences between the two stacks. In sample P13 (LSMO 40 nm) (see **Figure 14a**), the transition from LSMO to HZO is less sharp at the atomic level, showing a 1–2 nm interfacial region where lattice fringes gradually form rather than appearing immediately well-defined. Within this region, the HZO lattice planes display local bending, interruptions, and minor variations in spacing, indicating a structurally disordered or mixed-phase nucleation layer next to the electrode. The interface also appears slightly wavy at the scale of individual atomic planes, suggesting nanoscale roughness rather than a perfectly planar boundary.

In contrast, in sample P25 (deposited on LSMO = 20 nm) (see **Figure 17a**), the HZO/LSMO interface appears sharper: Well-ordered HZO lattice fringes are more directly aligned above the LSMO, and the boundary between the two layers remains straighter over several nanometers. Although local inhomogeneities are still observed, as expected for ultrathin HZO, the level of disorder and phase mixing at the immediate interface is lower compared to P13. These structural differences are reflected in the local phase distribution obtained from FFT/IFFT analysis. In P13, the initial few nanometers of HZO above the LSMO contain a higher proportion of monoclinic regions mixed with orthorhombic domains, whereas in P25, the orthorhombic component is more dominant near the interface and more coherently aligned across adjacent grains. Overall, these findings suggest that the more relaxed 40 nm LSMO electrode leads to a structurally less uniform and more defective interfacial HZO layer, while the strained 20 nm LSMO electrode supports a cleaner, more coherent nucleation environment that stabilizes a larger fraction of the ferroelectric orthorhombic phase.

Such an interfacial structural difference aligns with the observed reduction in effective capacitance and the increase in leakage for P13, as a structurally disordered interfacial layer can act as a low-quality dielectric in series with the bulk HZO.

The capacitance–frequency characteristics in **Figure 18(c)** show a significant difference between the two heterostructures: The P25 sample (with a 40 nm LSMO bottom electrode) exhibits capacitance values approximately twice those of the P13 sample (with a 20 nm LSMO electrode) over a wide frequency range. The pronounced low-frequency dispersion in the P13 sample’s capacitance–frequency response indicates a major contribution from leakage currents and interfacial trap states, consistent with reports of defective HZO interfaces in similar ferroelectric thin-film systems.

In the P13 sample, the dielectric loss factor approaches unity at 0.1 kHz, indicating that the current is mainly due to conduction processes rather than displacement

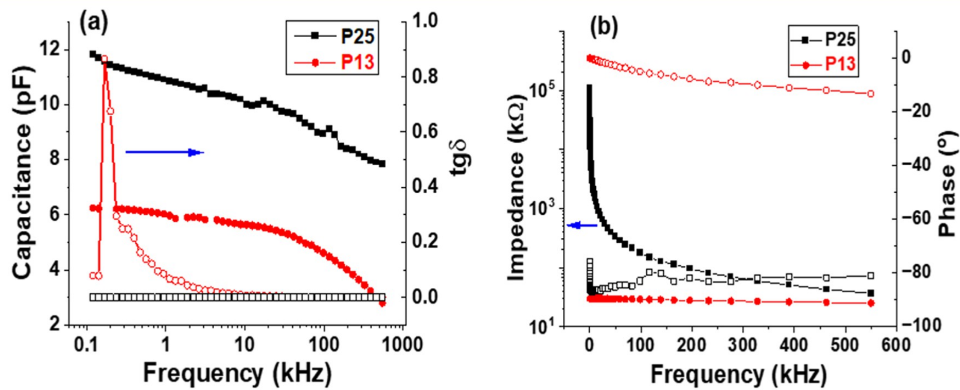


**Figure 18.**
*Frequency dependence of (a) capacitance (full symbols) and loss tangent (tgδ) (open symbols) and (b) impedance (full symbols) and phase angle (open symbols) for HZO/LSMO/STO capacitors with 40 nm (P13) and 20 nm (P25) LSMO bottom electrodes measured at room temperature.*

current. In contrast, the P25 sample shows significantly lower dielectric losses and reduced low-frequency dispersion, consistent with improved dielectric quality and a lower density of interfacial traps at the HZO/LSMO interface [33–37].

The impedance spectra (see **Figure 18(b)**) confirm that the P13 sample mainly acts as a leaky resistor in parallel with a capacitor, while the P25 sample displays primarily capacitive behavior across the measured frequency range. This indicates a much higher leakage resistance in P25 compared to P13.

The combined structural and electrical data clearly demonstrate a correlation between the nanoscale interfacial structure of the HZO/LSMO boundary and the overall ferroelectric response of the heterostructures. For the 40 nm LSMO bottom electrode (P13), partial strain relaxation of LSMO leads to a less coherent, more heterogeneous interfacial environment during HZO nucleation. High-resolution transmission electron microscopy shows a diffuse, locally disordered interfacial region extending over 1–2 nm, along with a higher fraction of monoclinic HZO and slight nanoscale undulations of the interface. These features promote defect formation, increase trap density, and lead to nonuniform local electric fields, which collectively cause increased dielectric losses, a lower effective capacitance, and a predominantly resistive impedance response dominated by leakage conduction. As a result, reliable ferroelectric switching could not be achieved in P13 under quasi-static triangular pulses because leakage masked the polarization current.

In contrast, the more strained and coherent 20 nm LSMO electrode (P25) provides a sharper and more uniform interfacial boundary for HZO growth. This promotes the stabilization of a larger fraction of the metastable orthorhombic phase near the interface, reduces structural disorder, and minimizes interfacial trap formation. Structurally, this is reflected in more continuous lattice fringes and a sharper HZO/LSMO transition in HRTEM. Electrically, these improvements lead to lower dielectric losses, higher effective capacitance, and a mainly capacitive impedance response. Consequently, clear ferroelectric switching was observed via PUND measurements (see **Figure 19**), resulting in a remanent polarization of approximately 20–25 μC $cm^{-2}$.

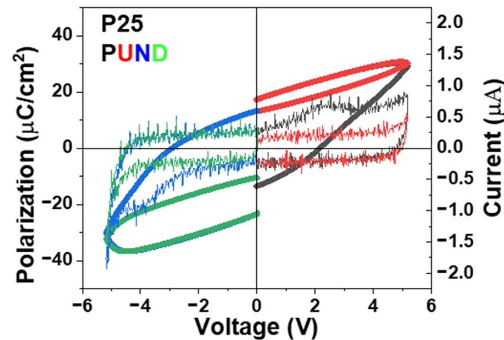


**Figure 19.**
*PUND polarization–voltage characteristics of the P25 sample (LSMO, 20 nm) measured with a triangular waveform at 1 kHz.*

## 4. Conclusions and outlook

The data presented in this chapter reveal that the functional behavior of both HZO and $Al_{1-x}Sc_xN$ thin films is governed by a complex relationship between electrical properties, preparation, and interface characteristics. The electrical performance of ultrathin epitaxial HZO is not solely determined by its thickness but also by the strain state and structural quality of the LSMO bottom electrode. Reducing the LSMO thickness from 40 nm to 20 nm induces significant changes in the microstructure and crystallographic texture of HZO, highlighting the critical role of the bottom electrode in determining the structural development of ferroelectric HZO films. We show that the ferroelectric performance of ultrathin HZO depends on film thickness but is also strongly controlled by the thickness of the LSMO bottom electrode, which governs the interfacial structure, the orthorhombic/monoclinic phase balance, and the competition between ferroelectric switching and leakage conduction.

For $Al_{1-x}Sc_xN$ thin films, XPS and electrical measurements highlight a critical materials challenge: Scandium doping, while essential for enhancing AlN's electrical parameters and functionality, also imposes significant constraints on crystallization and chemical stability (especially at the film's surface). X-ray photoelectron spectroscopy analysis shows that the ASN film exhibits significant surface oxidation dominated by Sc–O formation, with minor Al–O growth and traces of $N_2$. These signatures align with oxidation pathways reported in recent operando HAXPES studies. The discrepancy between surface and bulk stoichiometry, arising from preferential Sc oxidation and the limited information depth of XPS, indicates that surface chemistry must be considered when interpreting electrical measurements. The high oxygen affinity of ScN-AlN systems is a major challenge that can introduce parasitic resistive components, modify interface barrier heights, and alter the internal electric field distribution. Consequently, electrical characterization should be interpreted with caution, especially when evaluating films exposed to ambient conditions. These findings suggest that, for ASN thin films, proper capping strategies may be necessary to preserve the material's functional properties.

Key remaining challenges include (i) the narrow phase stabilization window, (ii) strong interface/surface chemistry effects, and (iii) the breakdown–coercive-field

trade-off that complicates reliable switching. These coupled trade-offs still hinder predictable integration across both material systems. In ultrathin HZO, the practical process window for stabilizing the ferroelectric orthorhombic phase is narrow because small variations in interface chemistry, strain state, and defect population can shift the orthorhombic/monoclinic balance while simultaneously amplifying leakage, thereby reducing the effective switching signal and increasing variability across nominally similar stacks. In $Al_{1-x}Sc_xN$, pushing toward switchable polarization by increasing Sc content must be balanced against phase stability and chemical robustness, while maintaining a breakdown field sufficiently above the coercive field; otherwise, premature breakdown, parasitic conduction paths (often promoted by surface oxidation), or field redistribution can dominate the measured response. Consequently, protocol-robust electrical characterization (cross-checking waveform dependence, separating switching from conduction, and controlling ambient exposure) becomes as important as materials optimization and defines key targets for future interface engineering and reliability studies, including endurance, imprint/fatigue, retention, and long-term stability.

Although experimental work over the last few years has shown progress in improving phase control and phase stabilization across both material systems, leakage currents remain a major limitation on device performance. Leakage currents are also common in other ferroelectric materials and degrade electrical properties, including remanent polarization, reducing fatigue resistance under repeated voltage cycling, limiting endurance, and, in some cases, leading to irreversible material degradation. Leakage current mechanisms depend strongly on thickness, defect structure, temperature, and interface configuration at the film/electrode interface, and one or more mechanisms can be present in the same sample. In ultrathin HZO films, interface-controlled conduction mechanisms, such as thermionic emission over the potential barrier at the electrode interface (Schottky emission), direct tunneling, electric field–assisted tunneling (Fowler–Nordheim tunneling), or a combination thereof, can dominate. In $Al_{1-x}Sc_xN$ films, where ferroelectricity is typically stabilized at larger thicknesses, bulk-controlled conduction mechanisms, including ohmic conduction, Poole–Frenkel emission from deep traps, space charge–limited currents, or hopping, can govern leakage currents. Therefore, for the integration of these materials into next-generation microelectronic devices, systematic studies to understand leakage current mechanisms, particularly the interplay among bulk defects, trap states, and interface barrier properties, are essential. A deeper understanding of how interface engineering, defect control, and heterostructure design influence the overall electrical response will be critical for improving reliability, endurance, and long-term device stability.

Overall, the outlook for CMOS-compatible ferroelectrics remains highly promising, yet progress toward large-scale deployment will be dictated less by the mere observation of switchable polarization and more by overcoming a common set of bottlenecks shared by these material classes, namely tight process windows, interface-driven variability, and reliability limits set by the competition between coercive and breakdown fields. Addressing these issues in a systematic, device-relevant manner through defect and interface control, combined with protocol-robust characterization, will be essential to translate the impressive laboratory demonstrations in HZO- and $Al_{1-x}Sc_xN$-based stacks into predictable and manufacturable technologies.

## Acknowledgments

The authors acknowledge financial support through the PNRR project 760239, dated December 28, 2023, funded by the Romanian Ministry of Research, Innovation, and Digitization through the National Recovery and Resilience Plan.

## Conflict of Interest

The authors declare no conflicts of interest.

## Author details

Luminița Mirela Hrib, Liliana-Marinela Balescu, Cristina Florentina Chirila, Andra-Georgia Boni, Dana Georgeta Popescu, Marian Cosmin Istrate, Roxana Elena Patru, Lucia Nicoleta Leonat and Lucian Pintilie
National Institute of Materials Physics, Măgurele, Romania

*Address all correspondence to: luminita.hrib@infim.ro

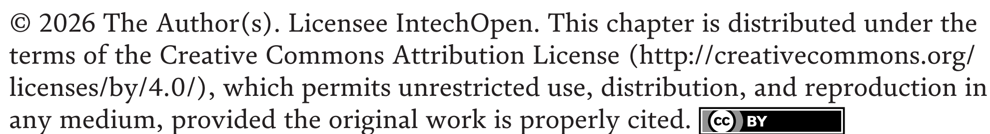

IntechOpen

© 2026 The Author(s). Licensee IntechOpen. This chapter is distributed under the terms of the Creative Commons Attribution License (http://creativecommons.org/licenses/by/4.0/), which permits unrestricted use, distribution, and reproduction in any medium, provided the original work is properly cited.

## References

[1] Rodriguez JA, et al. Reliability properties of low-voltage ferroelectric capacitors and memory arrays. IEEE Transactions on Device and Materials Reliability. 2004;**4**(3):436–449. DOI: 10.1109/TDMR.2004.837210

[2] Scott JF, de Araujo CAP. Ferroelectric memories. Science. 1989;**246**(4936):1400–1405. DOI: 10.1126/science.246.4936.1400

[3] Pintilie L, et al. Polarization induced self-doping in epitaxial Pb (Zr0.20Ti0.80)O3 thin films. Scientific Reports. 2015;**5**(1):14974. DOI: 10.1038/srep14974

[4] Lin B-T, Lu Y-W, Shieh J, Chen M-J. Induction of ferroelectricity in nanoscale ZrO2 thin films on Pt electrode without post-annealing. Journal of the European Ceramic Society. 2017;**37**(3):1135–1139. DOI: 10.1016/j.jeurceramsoc.2016.10.028

[5] Böscke TS, Müller J, Bräuhaus D, Schröder U, Böttger U. Ferroelectricity in hafnium oxide thin films. Applied Physics Letters. 2011;**99**(10):102903. DOI: 10.1063/1.3634052

[6] Năstase F, et al. Ferroelectric phase stabilization and Charge-Transport mechanisms in doped HfO2 thin films: Influence of Dopant Chemistry and Thickness. Coatings. 2025;**15**(12):1396. DOI: 10.3390/coatings15121396

[7] Xu X, et al. Kinetically stabilized ferroelectricity in bulk single-crystalline HfO2:Y. Nature Materials. 2021;**20**(6):826–832. DOI: 10.1038/s41563-020-00897-x

[8] Polakowski P, Müller J. Ferroelectricity in undoped hafnium oxide. Applied Physics Letters. 2015;**106**(23):232905. DOI: 10.1063/1.4922272

[9] Huan TD, Sharma V, Rossetti GA, Ramprasad R. Pathways towards ferroelectricity in hafnia. Physical Review B. 2014;**90**(6):064111. DOI: 10.1103/PhysRevB.90.064111

[10] Park MH, et al. Ferroelectricity and antiferroelectricity of doped thin HfO2-based films. Advanced Materials. 2015;**27**(11):1811–1831. DOI: 10.1002/adma.201404531

[11] Fichtner S, Wolff N, Lofink F, Kienle L, Wagner B. AlScN: A III-V semiconductor based ferroelectric. Journal of Applied Physics. 2019;**125**(11):114103. DOI: 10.1063/1.5084945

[12] Akiyama M, Kano K, Teshigahara A. Influence of growth temperature and scandium concentration on piezoelectric response of scandium aluminum nitride alloy thin films. Applied Physics Letters. 2009;**95**(16):162107. DOI: 10.1063/1.3251072

[13] Akiyama M, Kamohara T, Kano K, Teshigahara A, Takeuchi Y, Kawahara N. Enhancement of Piezoelectric response in scandium aluminum nitride alloy thin films prepared by dual reactive cosputtering. Advanced Materials. 2009;**21**(5):593–596. DOI: 10.1002/adma.200802611

[14] Leakage Mechanism and Cycling Behavior of Ferroelectric Al0.7Sc0.3N [Online]. Available from: https://www.mdpi.com/1996-1944/17/2/397 [Accessed: 2026-February-11]

[15] Schuster JC, Bauer J. The ternary systems ScAlN and YAlN. Journal of the Less Common Metals. 1985;**109**(2):345–350. DOI: 10.1016/0022-5088(85)90066-9

[16] Zhang Y, Zhu Q, Tian B, Duan C. New-generation ferroelectric AlScN Materials. Nano-Micro Letters. 2024;**16**(1):227. DOI: 10.1007/s40820-024-01441-1

[17] Tsai S-L, et al. Room-temperature deposition of a poling-free ferroelectric AlScN film by reactive sputtering. Applied Physics Letters. 2021;**118**(8):082902. DOI: 10.1063/5.0035335

[18] Li X, et al. Advanced growth techniques and challenges in ferroelectric AlScN thin films for next-generation electronic devices. Moore. More. 2025;**2**(1):10. DOI: 10.1007/s44275-024-00021-0

[19] Li M, Lin H, Hu K, Zhu Y. Oxide overlayer formation on sputtered ScAlN film exposed to air. Applied Physics Letters. 2022;**121**(11):111602. DOI: 10.1063/5.0106717

[20] Rehm O, et al. Long-term stability and oxidation of ferroelectric AlScN Devices: An operando hard X-ray photoelectron spectroscopy study. Physica Status Solidi (RRL) – Rapid Research Letters. 2025;**19**(3):2400307. DOI: 10.1002/pssr.202400307

[21] Ryoo SK, et al. Investigation of optimum deposition conditions of radio frequency reactive Magnetron sputtering of Al0.7Sc0.3N film with thickness down to 20 nm. Advanced Electronic Materials. 2022;**8**(11):2200726. DOI: 10.1002/aelm.202200726

[22] Tsai S-L, Hoshii T, Wakabayashi H, Tsutsui K, Kakushima K. A gradual change in Al1-XScX N Ferroelectric Film upon Switching Reversal. Meeting Abstracts. 2022;**MA2022-01**(29):1295. DOI: 10.1149/MA2022-01291295mtgabs

[23] Wang P, Wang D, Vu NM, Chiang T, Heron JT, Mi Z. Fully epitaxial ferroelectric ScAlN grown by molecular beam epitaxy. Applied Physics Letters. 2021;**118**(22):223504. DOI: 10.1063/5.0054539

[24] Messi F, Patidar J, Rodkey N, Dräyer CW, Trassin M, Siol S. Ferroelectric AlScN thin films with enhanced polarization and low leakage enabled by high-power impulse magnetron sputtering. APL Materials. 2025;**13**(5):051123. DOI: 10.1063/5.0267904

[25] Tsai S-L, et al. Field cycling behavior and breakdown mechanism of ferroelectric Al0.78Sc0.22N films. Japanese Journal of Applied Physics. 2022;**61**(SJ):SJ1005. DOI: 10.35848/1347-4065/ac54f6

[26] Kim KD, et al. Evolution of the ferroelectric Properties of AlScN film by electrical cycling with an inhomogeneous field distribution. Advanced Electronic Materials. 2023;**9**(5):2201142. DOI: 10.1002/aelm.202201142

[27] Derry GN, Ji-Zhong Z. Work function of Pt(111). Physical Review B. 1989;**39**(3):1940–1941. DOI: 10.1103/PhysRevB.39.1940

[28] Deng R, Evans SR, Gall D. Bandgap in Al1−xScxN. Applied Physics Letters. 2013;**102**(11):112103. DOI: 10.1063/1.4795784

[29] Solovan MN, Brus VV, Maistruk EV, Maryanchuk PD. Electrical and optical properties of TiN thin films. Inorganic Materials. 2014;**50**(1):40–45. DOI: 10.1134/S0020168514010178

[30] Sawa A. Resistive switching in transition metal oxides. Materials Today. 2008;**11**(6):28–36. DOI: 10.1016/S1369-7021(08)70119-6

[31] Dittmann R, Menzel S, Waser R. Nanoionic memristive phenomena in metal oxides: the valence change mechanism. Advances in Physics. 2021;**70**(2):155–349. DOI: 10.1080/00018732.2022.2084006

[32] Ielmini D. Resistive switching memories based on metal oxides: Mechanisms, reliability and scaling. Semiconductor Science and Technology. 2016;**31**(6):063002. DOI: 10.1088/0268-1242/31/6/063002

[33] Chaluvadi SK, et al. Epitaxial strain and thickness dependent structural, electrical and magnetic properties of La0.67Sr0.33MnO3 films. Journal of Physics D: Applied Physics. 2020;**53**(37):375005. DOI: 10.1088/1361-6463/ab8e7b

[34] Cheng X, et al. Leakage mechanism in ferroelectric Hf0.5Zr0.5O2 epitaxial thin films. Applied Materials Today. 2023;**32**:101804. DOI: 10.1016/j.apmt.2023.101804

[35] Toprasertpong K, Takenaka M, Takagi S. Breakdown-limited endurance in HZO FeFETs: Mechanism and improvement under bipolar stress. Frontiers in Electronics. 2022;**3**. DOI: 10.3389/felec.2022.1091343

[36] Benatti L, Vecchi S, Pesic M, Puglisi FM. The role of defects and interface degradation on Ferroelectric HZO capacitors aging. In: 2023 IEEE International Reliability Physics Symposium (IRPS), March. 2023; pp. 1–6. DOI: 10.1109/IRPS48203.2023.10118229

[37] Paul TK, Saha AK, Gupta SK. Oxygen Vacancy-Induced Monoclinic Dead Layers in Ferroelectric $Hf_xZr_{(1-x)}O_2$ With Metal Electrodes. arXiv: arXiv:2412.06416. 2024. DOI: 10.48550/arXiv.2412.06416